The Astrophysical Journal, 924:49 (8pp), 2022 January 10 https://doi.org/10.3847/1538-4357/ac31ad

Searching for Gravitationally Lensed Gamma-Ray Bursts with Their Afterglows

Shengnan Chen[1], Xudong Wen[2], He Gao[1], Kai Liao[2], Liangduan Liu[1], Litao Zhao[3], Zhengxiang Li[1], Marek Biesiada[1,4], Aleksandra Piórkowska-Kurpas[5], Shuo Xiao[6], and Shaolin Xiong[6]
[1] Department of Astronomy, Beijing Normal University, Beijing 100875, People's Republic of China; gaohe@bnu.edu.cn
[2] School of Science, Wuhan University of Technology, Wuhan 430070, People's Republic of China
[3] Department of Mathematics and Physics, Hebei GEO University, Shijiazhuang 050016, People's Republic of China
[4] National Centre for Nuclear Research, Pasteura 7, 02-093 Warsaw, Poland
[5] Institute of Physics, University of Silesia, 75 Pułku Piechoty 1, 41-500 Chorzów, Poland
[6] Institute of High Energy Physics (IHEP), Chinese Academy of Sciences (CAS), Beijing 100049, People's Republic of China
Received 2021 May 23; revised 2021 October 8; accepted 2021 October 19; published 2022 January 11

Abstract

Gamma-ray bursts (GRBs) at high redshifts are expected to be gravitationally lensed by objects of different mass scales. Other than a single recent claim, no lensed GRB has been detected so far by using gamma-ray data only. In this paper, we suggest that multiband afterglow data might be an efficient way to search for lensed GRB events. Using the standard afterglow model, we calculate the characteristics of the lensed afterglow lightcurves under the assumption of two popular analytic lens models: the point-mass and singular isothermal sphere models. In particular, when different lensed images cannot be resolved, their signals would be superimposed together with a given time delay. In this case, the X-ray afterglows are likely to contain several X-ray flares of similar width in linear scale and similar spectrum, and the optical afterglow lightcurve will show re-brightening signatures. Since the lightcurves from the image arriving later would be compressed and deformed in the logarithmic timescale, the larger time delay (i.e., the larger mass of the lens), the easier it is to identify the lensing effect. We analyzed the archival data of optical afterglows and found one potential candidate of the lensed GRB (130831A) with time delay ∼500 s; however, observations of this event in gamma-ray and X-ray bands seem not to support the lensing hypothesis. In the future, with the cooperation of the all-sky monitoring gamma-ray detectors and multiband sky survey projects, the method proposed in this paper would be more efficient in searching for strongly lensed GRBs.

Unified Astronomy Thesaurus concepts: Gamma-ray bursts (629)

1. Introduction

As one of the most violent explosions in the universe, gamma-ray bursts (GRBs) and their afterglows are bright enough to be detected in the high-redshift range up to at least $z \sim 10$ (Salvaterra et al. 2009; Tanvir et al. 2009). Due to their high redshift, the gravitational lensing effect on GRBs has long been discussed ever since the cosmological origin for GRBs was first proposed (Paczyński 1986). With detailed study on the probability distributions of time delay in gravitational lensing by point masses and isolated galaxies (modeled as singular isothermal spheres), Mao (1992) predicted that the probability of multiple GRB images being obtained from a galactic lensing event could be between 0.05% and 0.4%. And by assuming that the GRB luminosity function has no cosmological evolution and the lens is modeled as singular isothermal spheres, Hurley et al. (2019) estimated that the detection rate of both lensed GRB images is roughly 0.05 times per year.

Thanks to the successful operation of several dedicated detectors, e.g., the Burst And Transient Source Experiment (BATSE) on the Compton Gamma Ray Observatory (Meegan et al. 1992), the Burst Alert Telescope (BAT) on the Neil Gehrels Swift Observatory (Gehrels et al. 2004; Barthelmy et al. 2005), and the Gamma-Ray Burst Monitor (GBM) on the Fermi Observatory (Meegan et al. 2009), $\sim 10^4$ GRBs have been detected. Searches for gravitational lensing of GRBs have been widely carried out; for instance, Li & Li (2014) searched ∼2100 GRBs observed by BATSE, Hurley et al. (2019) searched ∼2300 GRBs observed by Konus-Wind, and Ahlgren & Larsson (2020) searched ∼2700 GRBs observed by GBM. In addition, Veres et al. (2009) and Davidson et al. (2011) also failed to search for lensing events with two smaller samples of GRBs observed in the first years of Fermi-GBM.

Unfortunately, all searches for galaxy lensing events (with time delay on the order of days) have yielded null results. Most recently, Paynter et al. (2021) claimed that they had found one statistically significant lensing event in the lightcurve of GRB 950830 (BATSE trigger 3770) with a sub-second time delay. The inferred lens mass, although depending on the unknown lens redshift, falls into the mass range of intermediate-mass black holes (e.g., $\sim 10^4$–$10^5 M_\odot$). The mismatch between theoretical predictions concerning lensing rates and the data search results might be due to the uncertainty of the theoretical model, or it may also be due to the fact that current gamma-ray detectors do not yet have all-sky monitoring (Li & Li 2014). Nevertheless, it is also possible that some real lensing events are missed in the data search process, considering that the current searches are mainly based on the comparison of gamma-ray lightcurves and the coincidence degree of positions. However, (1) the radiation timescale of GRBs in gamma-ray bands is relatively short, (2) the shape of lightcurve is greatly affected by the background, and (3) the positioning error of gamma-ray detectors is very large.

Here we propose that in addition to looking for lensed GRBs in the gamma-ray band, we can also search for them with GRB's afterglow observations, taking into account that the

afterglow's detectable timescale is much longer (up to years), their lightcurve shape is relatively simple, their physical model is much more clear, and they can be monitored by either satellites or ground-based multiband detectors in order to enhance the probability of capturing the lensing effect (Zhang 2018, for a review). For strongly gravitationally lensed events with lens mass M_l, the typical angular separation between multiple images could be roughly estimated as $0\farcs1(M_l/10^{10}M_\odot)^{1/2}(D_lD_s/D_{ls}/\mathrm{Gpc})^{-1/2}$ (Liao et al. 2020), which could hardly be resolved by facilities that are commonly used to observe GRB afterglows, unless the lens galaxy is extremely massive (e.g., $M_l > 10^{12}M_\odot$). For instance, the angular resolution of the Swift X-ray Telescope (XRT) is only 18″ (Burrows et al. 2005), and the resolution of 1 meter-class optical telescopes is ∼1″ (Oguri 2010). On the other hand, by studying the broad time delay probability distribution of the point lens, Mao (1992) found that the peak of the time delay probability appeared at 50 s ($M_l/10^6M_\odot$). Unlike the short-term gamma-ray emission, the detectable timescale for afterglows is typically much longer than the time delay timescale. In this case, if the multiple images are unresolved, the signals of multiple images will be superimposed—disguised as one signal.

In this paper, we first use the standard GRB afterglow and gravitational lensing models to calculate the lightcurve of such superimposed signals in different bands. Based on the characteristics of the calculated lightcurves, we then searched the current GRB afterglow observation data in the optical band. One potential candidate, GRB 130831A is found, and the possible parameter space is investigated in order to check if it is indeed a lensed event. Future prospects are discussed in the final section. Throughout this paper, we assume the Planck cosmology (Planck Collaboration et al. 2016) as a fiducial model, with $\Omega_\mathrm{m} = 0.307$, $\Omega_\Lambda = 0.693$, and $H_0 = 67$ km s^{-1} Mpc^{-1}.

2. GRB Afterglow Lightcurves with Unresolved Lensing Effect

2.1. GRB Afterglow Model

Although the nature of GRB's progenitor and central engine as well as the detailed physics of gamma-ray emission are still rather uncertain, a generic synchrotron external shock model has been well established to describe the interaction between the relativistic GRB jet and the circumburst medium, thus to interpret the broadband afterglow data (see Gao et al. 2013, for a review). The total effective kinetic energy of the jet and the medium can be expressed as

$$E_k = (\Gamma - 1)M_\mathrm{ej}c^2 + (\Gamma^2 - 1)M_\mathrm{sw}c^2, \quad (1)$$

where Γ is the bulk Lorentz factor of the outflow, and M_sw is the swept-up mass by the shock. The initial mass ejected from the central engine, M_ej, is a fixed value determined by $M_\mathrm{ej} = (E_0(1 - \cos\theta_0))/(\Gamma_0c^2)$, where E_0, Γ_0, and θ_0 are the initial total kinetic energy, initial bulk Lorentz factor, and the initial opening angle of the jet, respectively. Without considering the case of energy injection and energy loss due to shock emission, the differential form of energy conservation is given by (Huang et al. 2000)

$$\frac{d\Gamma}{dM_\mathrm{sw}} = -\frac{\Gamma^2 - 1}{M_\mathrm{ej} + 2\Gamma M_\mathrm{sw}}. \quad (2)$$

Applying the evolution expressions of M_sw, θ, and the radius R of the blastwave (Huang et al. 2000),

$$\frac{dM_\mathrm{sw}}{dR} = 2\pi R^2(1 - \cos\theta)m_pn, \quad (3)$$

where n is the number density of the circumburst medium,

$$\frac{d\theta}{dt} = \frac{c_s(\Gamma + \sqrt{\Gamma^2 - 1})}{R}, \quad (4)$$

and the sound speed c_s can be calculated as

$$c_s^2 = \frac{\hat{\gamma}(\hat{\gamma} - 1)(\Gamma - 1)}{1 + \hat{\gamma}(\Gamma - 1)}c^2, \quad (5)$$

where $\hat{\gamma}$ is the adiabatic index defined as $\hat{\gamma} = (4\Gamma + 1)/(3\Gamma)$,

$$\frac{dR}{dt} = \sqrt{\frac{\Gamma^2 - 1}{\Gamma}}c\Gamma(\Gamma + \sqrt{\Gamma^2 - 1}). \quad (6)$$

One can then solve the dynamical evolution of the external shock numerically. During the shock propagation, electrons are accelerated in the shock, which will radiate synchrotron emission in the magnetic fields behind the shock that are believed to be generated in situ due to plasma instabilities (Medvedev & Loeb 1999).

The electron energy distribution accelerated by shock is usually considered a power-law distribution: $N_{\gamma_e}d\gamma_e \propto \gamma_e^{-p}d\gamma_e$ ($p > 2$). Assuming that a constant fraction ϵ_e of the shock energy goes into the electrons, combined with electric neutral conditions and shock jump conditions, the minimum injected electron Lorentz factor can be estimated as (Sari et al. 1998)

$$\gamma_\mathrm{e,m} = \epsilon_e\left(\frac{p - 2}{p - 1}\right)\frac{m_p}{m_e}(\Gamma - 1). \quad (7)$$

Assuming a constant fraction ϵ_B of the shock energy density goes into the magnetic field, the magnetic field strength B' in the co-moving ejecta frame can be estimated as

$$B' \approx \sqrt{32\pi c^2\epsilon_B\Gamma^2m_pn}. \quad (8)$$

Synchrotron radiation power in the co-moving frame could then be calculated using the following formula (Rybicki & Lightman 1979):

$$P'_{\nu'} = \sqrt{3}\,\frac{q_e^3B'}{m_\mathrm{e}c^2}\int_{\gamma_\mathrm{e,m}}^{\gamma_\mathrm{e,M}}\left(\frac{dN_\mathrm{e}'}{d\gamma_\mathrm{e}}\right)F\left(\frac{\nu'}{\nu_\mathrm{cr}'}\right)d\gamma_\mathrm{e}, \quad (9)$$

where q_e is the electron charge, $\gamma_\mathrm{e,M}$ is the maximum electron Lorentz factor that could be estimated by balancing the acceleration timescale and the dynamical timescale, $\nu_\mathrm{cr}' = 3\gamma_\mathrm{e}^2q_eB'/(4\pi m_\mathrm{e}c)$ is the characteristic frequency of an electron with Lorentz factor γ_e, and

$$F(x) = x\int_x^{+\infty}K_{5/3}(k)dk, \quad (10)$$

where $K_{5/3}(k)$ is the modified Bessel function of the order of 5/3.

2.2. Gravitational Lensing Models

For the purpose of this work, we adopt two commonly used analytic lens models: the point-mass model and singular isothermal sphere (SIS) model. Their choice is dictated by two realistic scenarios: (1) lensing by an isolated mass—presumably a massive (with $M_l < 10^7 M_\odot$) black hole (BH), and (2) an intervening galaxy ($M_l \sim 10^9$–$10^{11} M_\odot$). We will not discuss the details of these scenarios here, as they are beyond the scope of this study.

In the case of axisymmetric point lenses, the typical separation between different images is set by the Einstein radius

$$\theta_{\rm E} = \sqrt{\frac{4GM_l}{c^2}\frac{D_{ls}}{D_l D_s}}, \tag{11}$$

where M_l is the mass of the lens, D_l is the angular diameter distance to the lens at redshift z_l, D_s is the angular diameter distance to the source at redshift z_s, D_{ls} is the angular diameter distance between the lens and the source. The dimensionless lens equation (Schneider et al. 1992) and its corresponding solutions are

$$y = x - \frac{1}{x} \rightarrow \begin{cases} x_+ = \dfrac{y + \sqrt{y^2+4}}{2} \\ x_- = \dfrac{y - \sqrt{y^2+4}}{2} \end{cases} \tag{12}$$

where $y = \beta/\theta_{\rm E}$, β denotes the angle between directions to the lens and to the source, and $x = \theta/\theta_{\rm E}$, where θ is the angular position of the image actually seen by the observer. Angular positions of the source and its images obey the lens equation: $\beta = \theta - \alpha$, where $\alpha = D_{ls}\hat{\alpha}/D_s$ is the reduced deflection angle. In the case of point-mass lenses, two images could be produced at angular positions $\theta_+ = x_+\theta_{\rm E}$ and $\theta_- = x_-\theta_{\rm E}$, respectively. The inverse of the determinant of the Jacobi matrix $\frac{\partial\beta}{\partial\theta}$ defines their magnifications,

$$\mu_\pm = \frac{1}{1 - \left(\frac{1}{x_\pm}\right)^4}. \tag{13}$$

The time delay between images produced by a point-mass lens is (Schneider et al. 1992):

$$\Delta t = \frac{4GM_l(1+z_l)}{c^3}\left(\frac{y\sqrt{y^2+4}}{2} + \ln\frac{\sqrt{y^2+4}+y}{\sqrt{y^2+4}-y}\right). \tag{14}$$

Point-mass lenses (also called Schwarzschild lenses) are representative to lensing by stars (microlensing) and BHs with stellar/intermediate mass.

It is well established that early-type galaxies act as lenses in the majority of strongly gravitationally lensed systems detected. Even though their formation and evolution are still not fully understood in detail, an SIS model can reasonably characterize the mass distribution of massive elliptical galaxies within the effective radius (Treu & Koopmans 2004; Treu et al. 2006; Cao et al. 2016; Liu et al. 2020). In the case of the axisymmetric SIS model (Narayan & Bartelmann 1996; Bernardeau 1999), its three-dimensional density profile could be described as $\rho(r) = \sigma_v^2/2\pi G r^2$, where r is the distance from the sphere center and σ_v is the velocity dispersion of the lens. By projecting the three-dimensional density along the line of sight, we obtain the corresponding surface density

$$\Sigma(\xi) = 2\frac{\sigma_v^2}{2\pi G}\int_0^\infty \frac{dz}{\xi^2+z^2} = \frac{\sigma_v^2}{2G\xi}, \tag{15}$$

where $\xi = \theta D_l$ is the impact parameter on the image plane. In this case, the dimensionless lens equation (Schneider et al. 1992) could be written as

$$y = x - \frac{x}{|x|}, \tag{16}$$

where $x = \xi/\xi_0$, $\xi_0 = 4\pi(\sigma_v/c)^2 D_l D_{ls}/D_s$ is the length scale on the lens plane, $y = \eta/\eta_0$, where $\eta = \beta D_s$ and $\eta_0 = \xi_0 D_s/D_l$ is the length scale related to ξ_0 on the source plane. There are two cases for the solution of the lens equation: when $y < 1$, the solutions are

$$x_\pm = y \pm 1. \tag{17}$$

The corresponding angular positions of the images are $\theta_\pm = \beta \pm \theta_{\rm E}$, where the Einstein radius $\theta_{\rm E}$ could be written as

$$\theta_{\rm E} = \sqrt{\frac{4GM(\theta_{\rm E})}{c^2}\frac{D_{ls}}{D_l D_s}} = 4\pi\frac{\sigma_v^2}{c^2}\frac{D_{ls}}{D_s}, \tag{18}$$

where $M(\theta_{\rm E})$ is the mass within the Einstein radius. In this case, the magnifications of the images are

$$\mu_\pm = 1 \pm \frac{1}{y}. \tag{19}$$

On the other hand, when $y > 1$, the lens equation only has one solution: $x = y + 1$. Its corresponding magnification is $\mu = |x|/(|x| - 1)$.

For the SIS model, the time delay between different images reads:

$$\Delta t = \frac{32\pi^2}{c}\left(\frac{\sigma_v}{c}\right)^4\frac{D_l D_{ls}}{D_s}(1+z_l)y. \tag{20}$$

2.3. Superposition of Lensed Images

When the lensed images are unresolved, our detected afterglow signal would be the superposition of signals from multiple images. In this case, the shape of the afterglow lightcurve depends on the number of images, their magnifications, and time delay between different images.

In the optical band, the afterglow lightcurve is mainly contributed to by the external shock emission. With the standard afterglow and gravitational lensing models as described above, we calculated some optical lightcurves of such superimposed signals in various scenarios. There are several free parameters involved in our calculations, which can be divided into two categories. The first category is associated with the external shock, including the initial kinetic energy of GRB outflow E_0, the initial bulk Lorentz factor of GRB outflow Γ_0, the initial opening angle of the jet θ_0, the equipartition parameters for the magnetic field and electrons: ϵ_B and ϵ_e, and the electron distribution index p. The second category is related to the lensing model, including the lens

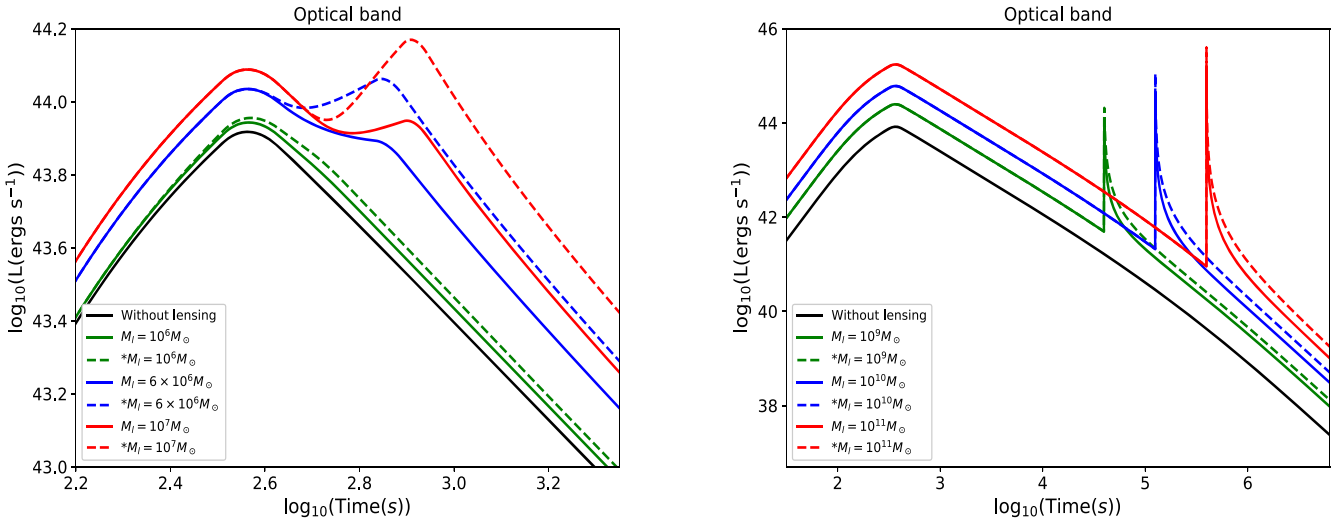

Figure 1. The lensed afterglow lightcurves in the optical band when the lens mass is less than $10^7 M_\odot$ (the left panel) and larger than $10^7 M_\odot$ (the right panel), respectively. Different from the right panel where $t_{\rm delay}$ is larger than $t_{\rm peak}$, the green, blue, and red lines in the left panel represent the cases where $t_{\rm delay}$ is smaller, equal, or larger than $t_{\rm peak}$, respectively. All dotted lines marked with * in the legend are the result of additional magnification (here we manually set the additional magnification factor as $\mu_{\rm add} = 2.5$) of the second image by the microlensing effect. The typical values for the model parameters are as follows: $E_0 = 10^{52}$ erg, $\Gamma_0 = 100$, $n = 1\ {\rm cm}^{-3}$, $\theta_0 = 0.1$, $\epsilon_e = 0.1$, $\epsilon_B = 10^{-4}$, $p = 2.5$, $z_l = 1$, $z_s = 2$, $\beta_{\rm point} = 1.8\theta_{\rm E}(M_l = 10^6 M_\odot)$, and $\beta_{\rm SIS} = 0.5\frac{\zeta_0}{D_l}(M_l = 10^9 M_\odot)$.

redshift z_l, the source redshift z_s, the angular position of the source β, and the lens mass M_l in the point-mass model and the SIS model. In the SIS model, mass within the Einstein radius is determined in the velocity dispersion and distance terms: $M_l = \frac{4\pi^2 c^2}{G}\left(\frac{\sigma_v}{c}\right)^4 \frac{D_{ls} D_l}{D_s}$.

For the purpose of this work, we first fix the parameters in the first category at their typical values, e.g., we set $E_0 = 10^{52}$ erg, $\Gamma_0 = 100$, $n = 1\ {\rm cm}^{-3}$, $\theta_0 = 0.1$, $\epsilon_e = 0.1$, $\epsilon_B = 10^{-4}$, and $p = 2.5$. With these settings, the afterglow lightcurves for each image are rather simple: corresponding to their own starting point, the lightcurve rises as t^2, peaks around $t_{\rm peak} \sim 360$ s, and then declines as $t^{-1.2}$.

By adjusting the values of parameters in the second category, we produced various scenarios with $t_{\rm delay}$ (delay time between different lensed images) being smaller, equal, or larger than $t_{\rm peak}$. As shown in Figure 1, when we take the initial time of the first image as the starting time, the lightcurves from the later-arriving image would be compressed and deformed in the logarithmic timescale, which would behave as a re-brightening signature. When the lens mass is relatively small (e.g., $M_l < 10^7 M_\odot$), $t_{\rm delay}$ is close to $t_{\rm peak}$. In this case, the re-brightening signature is not significant, unless the second image suffers additional magnification effects (such as microlensing). However, when the lens mass is large enough (e.g., $M_l > 10^7 M_\odot$), $t_{\rm delay}$ is much larger than $t_{\rm peak}$, and in this case, the re-brightening signature will have an extremely sharp rise, which would be very easy to identify.

Unlike the optical band, X-ray afterglow is a superposition of the conventional external shock component and a radiation component that is related to the late central engine activity, manifested through flares and extended shallow plateaus (Zhang et al. 2006). The lensing effect for the external shock component should be the same with the optical band (as shown in Figure 1). For the latter component, here we adopt the real observational data for GRB 160227A, which contains both X-ray flare and plateau, to simulate a pseudo-lightcurve to show the lensing effects for flares and plateaus. As shown in Figure 2, when $t_{\rm delay}$ is comparable to the timescale of early X-ray flares, the signal from the later-arriving image will be masked as new flare components, superimposed with the flare of the first image or separated into multiple independent flares. In this case, the plateau signal does not change obviously, but the overall flux increases a little higher. When $t_{\rm delay}$ is large enough, the early X-ray signal would be compressed into a narrow jump pulse with extremely sharp rising and declining, which would be easy to identify once it appears.

In the radio band, the afterglow lightcurve would peak at a relatively late timescale. When the lens mass is small, $t_{\rm delay}$ would be much smaller than $t_{\rm peak}$, and no obvious lensing feature would show up since signals of both images are in the rising stage and are relatively weak. On the other hand, when the lens mass is large enough to make $t_{\rm delay}$ close to or larger than $t_{\rm peak}$, the angular separation between multiple images could be larger than the angular resolution of radio telescopes. For example, the Very Large Array, with a minimum resolution of $0\farcs04$,[7] could in principle distinguish lensed GRB images when the lens mass is larger than $10^9 M_\odot$ (with $t_{\rm delay} > 10^4$ s), so that the afterglow lightcurve from different images could be decomposed instead of superimposed. In this case, one can search directly for strongly gravitationally lensed GRBs in radio imaging. For these reasons, we did not show the results for the radio band here.

3. Archive Data Searching for Lensed GRB Candidates in the Optical Band

Based on the predicted characteristics in Section 2.3, we analyze the optical band by searching for the presence of an additional signal due to gravitational lensing of GRBs. We extensively search for the optical data from published papers or from the Gamma-ray Coordinates Network Circulars if no published paper is available. We found 358 GRBs in total with optical observations being reported from 1997 February to 2020 December, including 308 GRBs having well-sampled optical lightcurves, which contain at least three data points,

[7] https://public.nrao.edu/telescopes/vla/

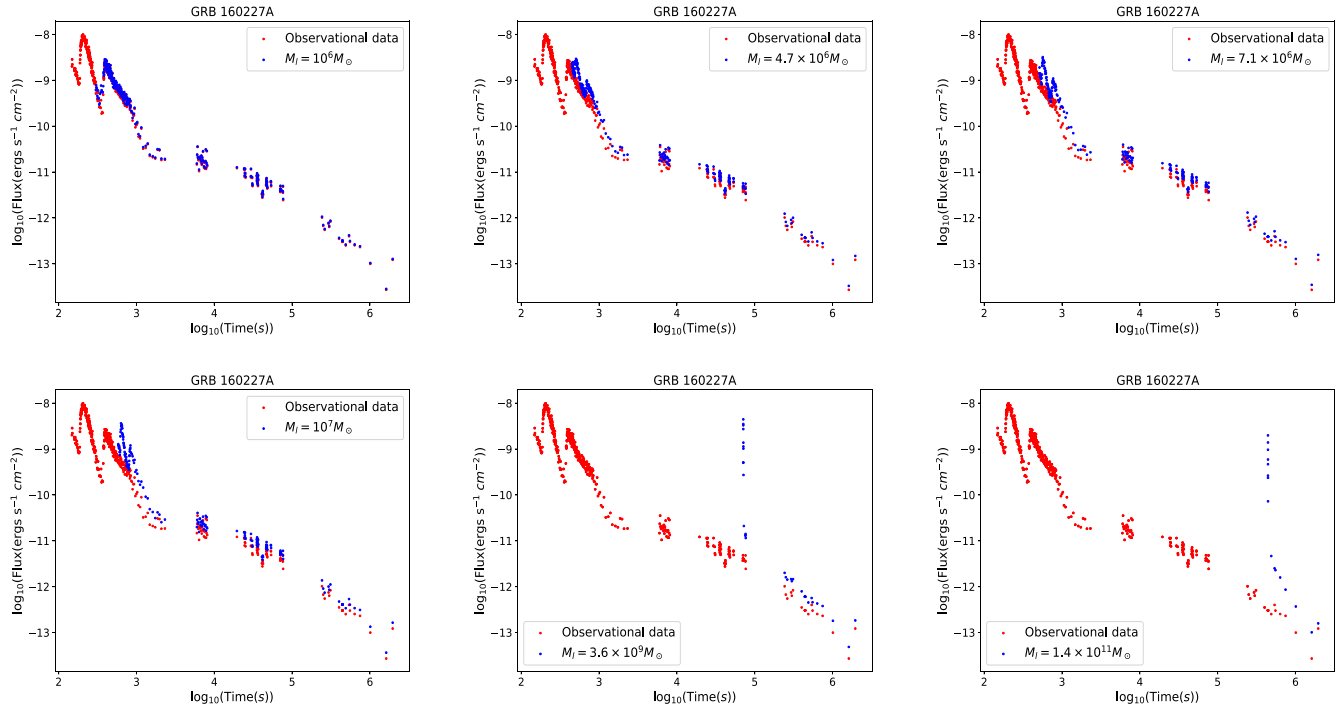

Figure 2. Simulation of gravitational lensing effect in X-ray afterglow of GRB 160227A. The observational data are marked with red dots. The blue dots are the result of the superposition from different lensed images after the second lensed image arrives. Here we set the flux from the first-arriving image equaling the observational data.

excluding upper limits.[8] By visual inspection, we systematically searched through our sample and identified three bursts that show a clear onset peak, followed by a steep re-brightening. These are GRB 100621A, GRB 100901A, and GRB 130831A. It is worth noting that some sources are also found to contain a steep re-brightening signature, but their early onset peak has not been observed (some examples are collected in de Ugarte Postigo et al. 2018). These sources together with GRB 100621A and GRB 100901A are further excluded because their re-brightening peak is too wide to be explained by the lensing effect; it's more like a giant bump caused by a fallback accretion process (Wu et al. 2013; Zhao et al. 2021). Overall, only one possible candidate is left: GRB 130831A with a redshift of 0.479 (Cucchiara & Perley 2013). De Pasquale et al. (2016) provided a comprehensive analysis for the ultraviolet, optical, and infrared photometry of GRB 130831A, whose combined optical lightcurves show a rapid temporal evolution between 400 and 800 s after the trigger (the optical flux suddenly increased by a factor of ∼5). The sharp rise feature is very difficult to explain within the external shock framework, unless invoking some complicated energy injection process, such as a continuously refreshed shock following the prompt emission phase (Zhang et al. 2016). De Pasquale et al. (2016) proposed that the sharp rising should be connected to internal dissipation processes, which occurred in the outflow, when the Lorentz factor is very high and relativistic effects cause rapid variations of the observed flux. We are interested here in testing whether the sharp rise feature is a signature of the lensing effect. Considering that the UV/optical/NIR data collected in De Pasquale et al. (2016) have not been corrected for Galactic and host-galaxy extinction, we use the *Rc*-band data of GRB 130831A provided by de Ugarte Postigo et al. (2018), which has been calibrated to the Vega system, corrected for Galactic extinction. In addition, the host galaxy and supernova have been subtracted.[9] We apply the model described in Section 2 to fit the data of GRB 130831A, by performing the χ^2 objective function minimization procedure with using the Markov Chain Monte Carlo method through the emcee code (Foreman-Mackey et al. 2013). In the fitting, we focus on the early observational data (e.g., $t < 1500$ s), which essentially reflects whether the lensing effect exists. In order to reduce the number of free parameters in our fitting, we fix several of them at their typical values. For instance, we set $E_0 = 10^{53}$ erg, $\theta_0 = 0.3$, $R_0 = 10^{15}$ cm, $\epsilon_e = 0.1$, and $\epsilon_B = 10^{-4}$. We take the initial bulk Lorentz factor Γ_0 of the outflow, the number density n of the circumburst medium, the magnifications of the two images (Mag_1, Mag_2), and the time delay between the two images t_{delay} as the free parameters. Note that by fitting the observed lightcurve, parameters characterizing the overall lensing effect (magnifications and time delay) can be obtained directly. The lens system parameters, such as M_l, z_l, and β, could hardly be resolved due to strong degeneracy, unless some of them (z_l or β) could be directly determined with observations. Figure 3 shows our best-fitting results for the lightcurve and the corresponding corner plot of the posterior probability distribution for the fitting. We can see that the early lightcurve of GRB 130831A could be well fitted with our proposed model. The best-fit parameter values at the 1σ confidence level are $\Gamma_0 = 206^{+13}_{-11}$, $n = 6.3^{+2.6}_{-2.2}$ cm^{-3}, $\mathrm{Mag}_1 = 4.1^{+0.8}_{-0.6}$, $\mathrm{Mag}_2 = 7.8^{+1.5}_{-1.2}$, and $t_{\mathrm{delay}} = 492^{+3.5}_{-3.6}$ s. Constraints on all parameters associated with the external shock are consistent with typical values. Note that due to the lack of information about the baseline (unlensed) flux, the values of

[8] Part of our sample has been published in the literature (e.g., Li et al. 2012; Wang et al. 2015).

[9] Note that GRB 130831A is known to be associated with SN 2013fu (Cano et al. 2014). The *Rc*-band data we used here has subtracted the supernova contribution.

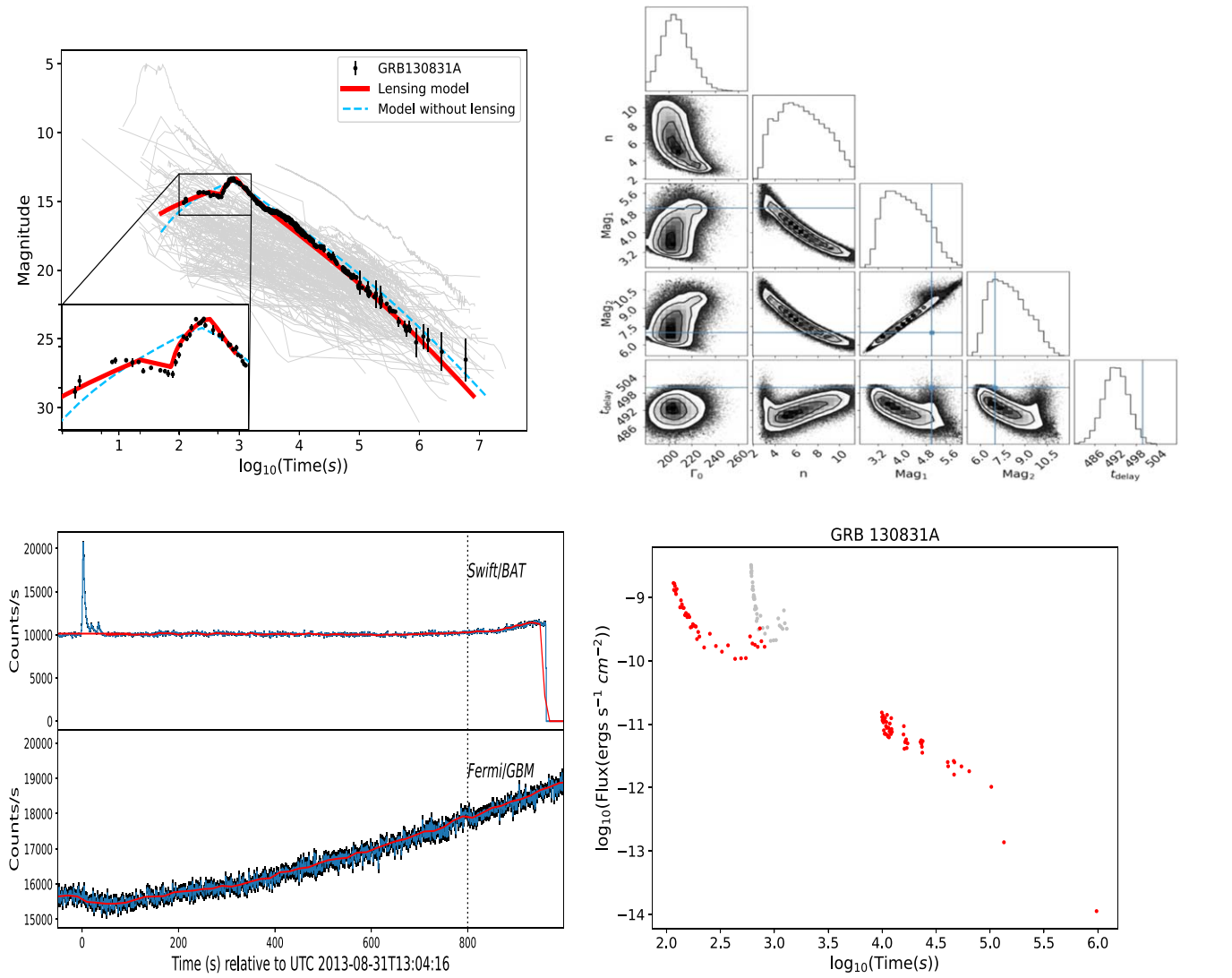

Figure 3. Top panels: the best-fitting results for the GRB 130831A optical afterglow, the corresponding corner plot of the posterior probability distribution for the fitting. The gray background lines show the optical lightcurves collected in our sample. Bottom panels: gamma-ray and X-ray band observations of GRB 130831A, where red lines in the left panel present the background level. In the plot of X-ray observation, for comparison, we manually shift the early X-ray data by $t_{\rm delay} = 492$ s and $\rm Mag_2/Mag_1 = 1.9$ to show the expected flux level around the time when the second optical peak emerges (see gray dots in the right panel).

$\rm Mag_1$ and $\rm Mag_2$ should be highly degenerated with the afterglow modeling parameters, so that the ratio between $\rm Mag_1$ and $\rm Mag_2$ is more meaningful, compared with their absolute values. According to the constraint result, the time delay between the two lensed images is $\sim$500 s, and the flux ratio is $\sim$2. Through external interpolation, we show that the best-fitting lightcurve is generally consistent with the late time observations.[10] For completeness, we also fit the early data of GRB 130831A by using the standard afterglow model without invoking any lensing effect, and the best-fit result is shown in Figure 3 as well. We then use the Bayesian method to test how significant the observation supports the lensing model (marked as model M_1) against the model without strong lensing (marked as model M_2). It turns out the lensing model is more preferable by the observations (see the Appendix for details of our adopted Bayesian method and relevant results).

However, it is worth noting that although the optical data of GRB 130831A can be well fitted by the lens effect, it is highly doubtful whether the source is actually lensed for the following reasons:

1. The second arriving image has a larger magnification. Usually, for typical lens models, if there are only two lensed images, the second image should be fainter, as the echo. In other words, even if GRB 130831A is actually lensed, it may have experienced very special gravitational lensing events. One possible lens model is a point-mass +shear, which might explain the brighter trailing images (Chen et al. 2021). Another plausible explanation for such a particular combination of time delay and the flux ratio could be the existence of a dark matter subhalo of mass $\sim 10^6 M_\odot$ in the galaxy resulting in the obtained value of time delay. In this case the magnification of the second image (and estimated value of the flux ratio) could

[10] Between 3000 s and 17000 s, the observational data show a plateau feature, which makes this part of the data slightly higher than the extrapolation extension of the best-fitting lightcurve. This is acceptable since the plateau feature is likely related to the late central engine activity (see De Pasquale et al. 2016 for detailed physical interpretations for late time observations of GRB 130831A).

be caused by a microlensing effect, i.e., by the stars in the lens galaxy. Let us note that microlensing effect on GRB afterglows has been discussed in some previous works (e.g., Gaudi & Loeb 2001; Ioka & Nakamura 2001; Koopmans & Wambsganss 2001).

2. Since GRB 130831A was triggered by Swift, we checked the historical data of BAT and XRT. As shown in Figure 3, when the second optical peak emerges, there is no signal showing up in the BAT data. Before the data recording stopped, the BAT data did show an increasing trend, but it is difficult to judge whether it is a real signal or it is caused by satellite attitude adjustment. There is an X-ray flare starting at about 500 s after the trigger, which is roughly consistent with the optical rising feature, but the flux at ∼800 s is about an order of magnitude lower than the flux at ∼100 s, inconsistent with the expected magnification ratio. We also checked the historical data of Fermi/GBM and found that the position of GRB 130831A was blocked by the Earth at the trigger time, but it entered the monitoring region of GBM after hundreds of seconds. As shown in Figure 3, when the second optical peak was emerging, there were no signals showing up in the GBM data. Interestingly, the GBM data also showed an obvious rise around the time when the second optical peak emerged. However, this may be caused by the rise of the background, because data in all of the detectors of GBM have risen, and the satellite has entered the high latitude region in that period.

4. Discussion and Conclusion

It has long been proposed that GRBs have the potential to be gravitationally lensed into multiple images, due to their high-redshift nature. The detection of lensed GRBs could be used to improve constraints on cosmological parameters such as the Hubble constant H_0, to test fundamental physics from the propagation speed, and to make constraints on the abundance of compact dark matter, and so on (Oguri 2019, for a review).

The traditional searches for lensed GRBs are focused on the gamma-ray band. Here we propose that one can search for lensed GRBs by combining gamma-ray and the multiband afterglow data. We use the standard afterglow model and two standard lens models to calculate the characteristics of the lensed afterglow lightcurves in different scenarios concerning lens mass and time delays. Based on our results, we suggest that the future search for lensed GRBs should be focused on the following cases: (1) When a lens is a compact object, the time delay is on the order of ∼100 s or less. In this case, multiple gamma-ray images could be either separated or overlapped, depending on the comparison between T_{90} and $t_{\rm delay}$. It is also possible that only one image signal can be seen, once the later-arriving signal is under the detector threshold. In this case, we can use the observation of X-ray and optical afterglow data to judge whether these GRBs are lensed or they just happen to have several similar emission episodes. If the GRBs are indeed lensed, the X-ray afterglows are likely to contain several X-ray flares with similar width in linear scale (the later, the narrower in logarithmic scale) and similar spectrum. Moreover, the optical afterglow lightcurve will show re-brightening signatures. (2) When the compact object is a low-mass galaxy, the time delay would be $\sim 10^3$–10^4 s. In this case, there will be two independent GRB triggers in the gamma-ray band, and there will be a sharp rise flare feature in both the X-ray and optical afterglow lightcurve, which can help to easily justify the lensing effect. (3) When the compact objects are massive galaxies, the time delay would be on the order of days or even longer. In this case, there will be two independent GRB triggers in the gamma-ray band, and the late X-ray signal will rise sharply. Nevertheless, optical telescopes now usually have the ability to resolve different lensed images, so as to better help confirm the lensing effect. Note that for all three situations, radio telescopes usually have the ability to resolve multiple images. Therefore, for suspected samples selected from the gamma-ray, X-ray, and optical bands, concerted radio observations could finally help to confirm whether they are real lensing events.

Through archived data searching in the optical band, we find one potential candidate of a lensed GRB, 130831A, with a time delay ∼500 s, which should belong to the first situation we discuss above. However, the gamma-ray and X-ray band observations of GRB 130831A seem to not support the lensing hypothesis. Therefore, whether this source is a lensed event remains to be further discussed. With the successful operation of many sky survey projects in multiple bands, especially the establishment of all-sky gamma-ray monitors, more lensed GRBs would be detected and accurately certified in the future.

Table 1
Prior Probability Distributions Adopted in the Bayesian Analysis, and the Natural Logarithm of Bayes Factor Calculated by `dynesty` for M_1 and M_2, Where $\mathcal{U}$ and $\mathcal{G}$ Refer to the Uniform and Gaussian Types of Prior, Respectively

	P1	P2	P3
Γ_0	$\mathcal{U}(100, 300)$	$\mathcal{U}(100, 500)$	$\mathcal{G}(200, 40)$
n	$\mathcal{U}(0, 5)$	$\mathcal{U}(0, 50)$	$\mathcal{G}(10, 5)$
Mag_1	$\mathcal{U}(0, 6)$	$\mathcal{U}(0, 6)$	$\mathcal{U}(0, 6)$
Mag_2	$\mathcal{U}(0, 12)$	$\mathcal{U}(0, 12)$	$\mathcal{U}(0, 12)$
$t_{\rm delay}$	$\mathcal{U}(450, 550)$	$\mathcal{U}(450, 550)$	$\mathcal{U}(450, 550)$
$\ln(\mathrm{BF}^1_2)$	589	596	597

We thank Dr. David Alexander Kann for sharing with us the data of GRB 130831A. We thank the anonymous referee for the helpful comments that have helped us to improve the presentation of the paper. This work is supported by the National Natural Science Foundation of China (NSFC) under grant Nos. 11690024, 12021003, 11633001, and 11973034.

Appendix

Here we employ the `dynesty` nested sampling algorithm (Skilling 2012) implemented in `bilby` (Ashton et al. 2019) to calculate the Bayes factor

$$\mathrm{BF}^1_2 = \frac{\mathcal{Z}_1(d|M_1)}{\mathcal{Z}_2(d|M_2)}, \tag{A1}$$

where $\mathcal{Z}_{1,2}$ is the evidence of model $M_{1,2}$, which can be estimated as

$$\mathcal{Z}(d|M) = \int \mathcal{L}(d|\theta, M)\pi(\theta|M)d\theta, \tag{A2}$$

where $\mathcal{L}$ is the likelihood and π is the prior of parameters. Here we choose Gaussian likelihood and three different prior cases (P1, P2 and P3) for both M_1 and M_2. The results are shown in

Table 1. It turns out $\ln(BF_2^1)$ between the lensing and non-lensing models could be as large as ∼600, and this result is not sensitive to the choice of prior. Normally when $\ln(BF_2^1)$ is larger than eight, one can conclude that the M_1 model is significantly favored against the M_2 model (Mackay 2003). In our case, it is clear that the lensing model is more preferable by the optical observations. In order to check the results from `dynesty`, we also calculated $\ln(BF_2^1)$ by using other public codes, such as `ptemcee` (Foreman-Mackey et al. 2013; Vousden et al. 2016), whose results are consistent with the result from `dynesty`. The seemingly excessive large number of $\ln(BF_2^1)$ should come from two reasons: (1) for the early data, the difference between the two models is significant, which can be clearly seen from the subgraph inserted in Figure 3; and (2) the Bayes factor crucially depends on the error of observational data points (see detailed illustrations and examples in John 2005), so that the relatively small error for early data points could lead to the huge $\ln(BF_2^1)$ value.

ORCID iDs

He Gao https://orcid.org/0000-0002-3100-6558
Litao Zhao https://orcid.org/0000-0001-6437-0869
Marek Biesiada https://orcid.org/0000-0003-1308-7304
Shuo Xiao https://orcid.org/0000-0003-2957-2806
Shaolin Xiong https://orcid.org/0000-0002-4771-7653

References

Ahlgren, B., & Larsson, J. 2020, ApJ, 897, 178A
Ashton, G., Hübner, M., Lasky, P. D., et al. 2019, ApJS, 241, 27
Barthelmy, S. D., Barbier, L. M., Cummings, J. R., et al. 2005, SSRv, 120, 143
Bernardeau, F. 1999, Theoretical and Observational Cosmology, Vol. 541 (Dordrecht: Kluwer), 179
Burrows, D. N., Hill, J. E., Nousek, J. A., et al. 2005, SSRv, 120, 165
Cano, Z., de Ugarte Postigo, A., Pozanenko, A., et al. 2014, A&A, 568, A19
Cao, S., Biesiada, M., Yao, M., & Zhu, Z.-H. 2016, MNRAS, 461, 2192
Chen, X., Shu, Y., Zheng, W., et al. 2021, ApJ, 912, 134
Cucchiara, A., & Perley, D. 2013, GCN, 15144, 1
Davidson, R., Bhat, P. N., & Li, G. 2011, in AIP Conf. Proc. 1538, Gamma Ray Bursts 2010, ed. J. E. McEnery, J. L. Racusin, & N. Gehrels (Melville, NY: AIP), 17
De Pasquale, M., Oates, S. R., Racusin, J. L., et al. 2016, MNRAS, 455, 1027
de Ugarte Postigo, A., Thöne, C. C., Bensch, K., et al. 2018, A&A, 620, A190
Foreman-Mackey, D., Hogg, D. W., Lang, D., & Goodman, J. 2013, PASP, 125, 306
Gao, H., Lei, W.-H., Zou, Y.-C., et al. 2013, NewAR, 57, 141
Gaudi, B. S., & Loeb, A. 2001, ApJ, 558, 643
Gehrels, N., Chincarini, G., Giommi, P., et al. 2004, ApJ, 611, 1005
Huang, F. Y., Gou, L. J., Dai, Z. G., et al. 2000, ApJ, 543, 90
Hurley, K., Tsvetkova, A. E., Svinkin, D. S., et al. 2019, ApJ, 871, 121
Ioka, K., & Nakamura, T. 2001, ApJ, 561, 703
John, M. V. 2005, ApJ, 630, 667
Koopmans, L. V. E., & Wambsganss, J. 2001, MNRAS, 325, 1317
Li, C., & Li, L. 2014, SCPMA, 57, 1592
Li, L., Liang, E.-W., Tang, Q.-W., et al. 2012, ApJ, 758, 27
Liao, K., Zhang, S.-B., Li, Z., et al. 2020, ApJL, 896, L11
Liu, T., Cao, S., Zhang, J., et al. 2020, MNRAS, 496, 708
MacKay, D. J. C. (ed.) 2003, Information Theory, Inference and Learning Algorithms (Cambridge: Cambridge Univ. Press), 640
Mao, S. 1992, ApJL, 389, L41
Medvedev, M. V., & Loeb, A. 1999, ApJ, 526, 697
Meegan, C., Lichti, G., Bhat, P. N., et al. 2009, ApJ, 702, 791
Meegan, C. A., Fishman, G. J., Wilson, R. B., et al. 1992, Natur, 355, 143
Narayan, R., & Bartelmann, M. 1996, in Formation of Structure in the Universe —Proc. 1995 Jerusalem Winter School, ed. A. Dekel & J. P. Ostriker (Cambridge: Cambridge Univ. Press)
Oguri, M. 2010, PASJ, 62, 1017
Oguri, M. 2019, RPPh, 82, 12901
Paczyński, B. 1986, ApJL, 308, L43
Paynter, J., Webster, R., & Thrane, E. 2021, NatAs, 5, 560
Planck Collaboration, Ade, P. A. R., Aghanim, N., et al. 2016, A&A, 594, A13
Rybicki, G. B., & Lightman, A. P. 1979, Radiative Processes in Astrophysics (New York: Wiley)
Salvaterra, R., Della Valle, M., Campana, S., et al. 2009, Natur, 461, 1258
Sari, R., Piran, T., Narayan, R., et al. 1998, ApJL, 497, L17
Schneider, P., Ehlers, J., & Falco, E. E. 1992, Gravitational Lenses (Berlin: Springer)
Skilling, J. 2012, in AIP Conf. Proc. 1443, 31st Int. Workshop on Bayesian Inference and Maximum Entropy Methods in Science and Engineering, ed. P. Goyal et al. (Melville, NY: AIP), 145
Tanvir, N. R., Fox, D. B., Levan, A. J., et al. 2009, Natur, 461, 1254
Treu, T., & Koopmans, L. V. E. 2004, ApJ, 611, 739
Treu, T., Koopmans, L. V. E., Bolton, A. S., Burles, S., & Moustakas, L. A. 2006, ApJ, 650, 1219
Veres, P., Bagoly, Z., Horvath, I., et al. 2009, arXiv:0906.1578
Vousden, W. D., Farr, W. M., & Mandel, I. 2016, MNRAS, 455, 1919
Wang, X.-G., Zhang, B., Liang, E.-W., et al. 2015, ApJS, 219, 9
Wu, X.-F., Hou, S.-J., & Lei, W.-H. 2013, ApJL, 767, L36
Zhang, B. 2018, The Physics of Gamma-Ray Bursts (Cambridge: Cambridge Univ. Press)
Zhang, B., Fan, Y. Z., Dyks, J., et al. 2006, ApJ, 642, 354
Zhang, Q., Huang, Y. F., & Zong, H. S. 2016, ApJ, 823, 156
Zhao, L., Gao, H., Lei, W., et al. 2021, ApJ, 906, 60